RSC Advances

PAPER

View Article Online
View Journal | View Issue

Cite this: *RSC Adv.*, 2026, **16**, 22794

Synergetic design of a sulfonated polyimide matrix anchored with phosphotungstic acid-loaded MOFs for enhanced fuel cell efficiency

Ragasudha Sudhakaran, Preethi Dayalan and Paradesi Deivanayagam *

Received 2nd March 2026
Accepted 17th April 2026

DOI: 10.1039/d6ra01800a

rsc.li/rsc-advances

The H_2–O_2 fuel cell performance of the synthesised sulfonated polyimide (sPI) membrane is significantly enhanced by incorporating a phosphotungstic acid-loaded MOF matrix into the polymer. The sPI polymer is synthesized using a chemical imidization method from its monomers. Herein, we prepare immobilized phosphotungstic acid on the metal organic frameworks of iron (HPW@MIL-100(Fe)) *via* a hydrothermal process. Composite membranes with varying filler loadings are fabricated using a solution-casting technique. The polymer sPI/HPW@MIL-100(Fe) composites exhibit enhanced physicochemical and electrochemical properties, surpassing those of the pristine sPI membrane. The electrostatic interactions between the polymer functionalities and the filler units are responsible for their performance in fuel cell applications. The membrane loaded with 4 wt% HPW@MIL-100(Fe) exhibits a high water uptake and ion exchange capacity of 21.86% and 1.92 meq per g, respectively. The proton conductivity reached 0.085 S cm^{-1} for this composite, but the performance declined beyond this loading due to aggregation. The fabricated MEA with 4 wt% HPW@MIL-100(Fe) delivers a power density of 216 mW cm^{-2} during fuel cell testing. The resultant power output from the sPI/HPW@MIL-100(Fe) electrolyte membrane can be used for stationary applications operating within 150–220 mW cm^{-2} power density range.

1. Introduction

The world is facing a severe energy crisis due to the rising population, which is often viewed as a form of poverty. To eradicate this issue, world leaders at the UN Summit adopted Sustainable Development Goal 7 (SDG 7), which focuses on the theme 'Affordable and Clean Energy'. This goal aims to develop energy-producing technologies that are viable and highly efficient in a greener manner. In addition, this goal promotes the use of renewable energy sources, such as solar, wind, geothermal, nuclear, and electrochemical energy systems, like fuel cells and batteries, for energy production. Practical difficulties, such as storage, transportation, and unpredictability, have hindered the advancement of renewable energy systems and increased the demand for fuel cells and batteries. In fuel cells, oxidation and reduction reactions at the anode and cathode produce electricity and water as the major byproducts. Among the various types of fuel cells, polymer electrolyte membrane fuel cells (PEMFCs) are considered highly efficient due to their potential properties, including low emissions of harmful effluents, quiet operation, and a consistent source of power generation in remote areas. Furthermore, their prevalence has been notable due to their high-power density and ability to operate at higher temperature conditions.[1–3]

To date, hydrophobic and hydrophilic backbones possess a perflurosulfonated membrane. Nafion is considered the standard PEM membrane. Its superior thermal and mechanical stability, along with its good proton conductivity, make Nafion a state-of-the-art PEM material. However, its high cost and poor performance at elevated temperatures hinder its utilization in academic and industrial applications.[4] Biopolymers like chitosan[5] and alginates[6] were initially explored as PFSA alternatives. The low cost and renewability of these materials have made them more appealing, but their low performance and durability have limited their use. Aromatic backbone polymers, such as sulfonated polyether ether ketone (SPEEK),[7] sulfonated polyether sulfone (SPES),[8] polybenzimidazole (PBI),[9] and sulfonated polyimide (sPI),[10] have been examined and are considered the best alternatives to Nafion.

The imide ring backbone of polyimide contributes to its high thermal stability, mechanical strength, and chemical resistivity, which has attracted special attention to polyimide polymers in recent years.[11] Direct polymerization using sulfonated diamine with anhydride is a straightforward method for synthesizing sulfonated polyimides.[12] In the case of post-sulfonation, there is a high possibility of imide hydrolysis, which adds to the justification for using PI synthesis *via* the pre-sulfonation process.[13] The proton conductivity and performance of the sulfonated

Department of Chemistry, Faculty of Engineering and Technology, SRM Institute of Science and Technology, Kattankulathur, Chengalpattu District, Tamil Nadu, 603203, India. E-mail: paradesd@srmist.edu.in

polyimide are highly influenced by the diamine and anhydride moieties. Six-membered anhydrides have longer fuel cell durability than five-membered polyimides, and flexible diamines like ODADS increase the oxidative stability of the polyimides, which is the reason for choosing NTDA-ODADS-based polyimides.[14] In addition, the presence of bulky substituents in the non-sulfonated diamine, like BAPP, facilitates the formation of an open structure by preventing regular, close, parallel polymer packing. This tailor-made structure enhances conductivity even under lower humidity conditions.[15] The physicochemical and electrochemical properties of the bare polymer can be improved by adding fillers, like metal oxides,[16] heteropolyacids,[17] carbon nanotubes,[18] ionic liquids,[19] and metal–organic frameworks.[20]

Heteropolyacids, also known as heteropoly electrolytes, are defined by the term 'green catalysts' due to their high stability, selectivity, non-corrosive properties, and extended lifetime in solution.[21] Without any external support, heteropoly acids can act as effective proton conductors because of their hydrophilicity, which helps to hold water and maintain super acidity, rapidly migrating protons between adjacent polyanions.[22,23] S. M. J. Zaidi *et al.*[24] developed a SPEEK/HPA composite membrane that showed enhanced activity compared to neat SPEEK. The composite exhibits higher water uptake and proton conductivity values, which are attributed to the continuous aqueous phase and the Grotthuss reorientation mechanism facilitated by the heteropolyacid unit in the composite. Payam Molla-Abbasi and coworkers[25] developed a novel carbon nanotube-doped phosphotungstic acid incorporated with Nafion to improve performance. The expected outcome in terms of water uptake and conductivity was achieved due to the presence of acidic groups in phosphotungstic acid. This acidic functionality significantly enhanced the overall performance, establishing heteropolyacids as a promising platform for researchers to work with.

Heteropolyacids can be utilized in a variety of applications, but their low specific surface area, curtailed catalytic stability, high solubility, and leaching issues in aqueous solutions have hindered their use.[21] To overcome this, the HPA moiety must be encapsulated within the pores of metal–organic frameworks, thereby leveraging their high porosity.[26] Zhenguo Zhang and colleagues[27] are the first to report phosphotungstic acid encapsulated MIL-100(Fe) loaded with sulfonated poly (arylene ether ketone sulfone) containing carboxyl group (C-SPAEKS) matrix for PEMFC application. The 4% content-loaded composite exhibited a maximum proton conductivity of 0.072 S cm^{-1} at 80 °C, which is 1.8 times greater than that of pristine SPAEKS.

In this study, a new sulfonated polyimide (sPI) was prepared by applying the chemical imidization method, and HPW@MIL-100(Fe) was synthesized by applying the hydrothermal method. The van der Waals volume of the hydrothermally stable HPW (~13 Å) is larger than the size of the pentagonal window (5.5 Å) and hexagonal window (8.6 Å) of MIL-100(Fe), which reduces the risk of leaching. The incorporation of HPW@MIL-100(Fe) into the pristine sulfonated matrix facilitates the acid–acid interactions between the $-SO_3H$ of the polymer and the $-PO_3H$ of the filler. This functional group interaction paves additional pathways for proton conduction and transport. In this study, the thermal, physicochemical, mechanical, and electrical properties of the sPI/HPW@MIL-100(Fe) membranes were thoroughly investigated and discussed in detail.

2. Experimental section

2.1 Materials and methods

Naphthalene-1,4,5,8-tetracarboxylic dianhydride (NTDA) and benzene-1,3,5-tricarboxylic acid were purchased from Sigma-Aldrich. 4,4′-oxydianiline (ODA), 2,2-bis[4-(4-aminophenoxy) phenyl]propane (BAPP) and isoquinoline were acquired from BLD Pharm Laboratories, India. Iron(III) chloride hexahydrate, benzoic acid, triethylamine (Et_3N), *m*-cresol, hydrochloric acid, dimethyl sulfoxide, *N*,*N*-dimethylformamide, acetone, phosphotungstic acid and concentrated sulfuric acid (97%) were purchased from Sisco Research Laboratories Pvt. Ltd, India. Fuming sulfuric acid (20%) was procured from Spectrochem Pvt. Ltd, India. NTDA and benzoic acid were vacuum dried at 160 °C for 20 h and 80 °C for 24 h, respectively, before use. Et_3N and *m*-cresol were dried over 4-Å molecular sieves prior to use. All other chemicals were used as received without further purification.

2.2 Synthesis of sulfonated polyimide (sPI)

The synthesis of the sPI polymer was carried out using a method reported previously by our team.[14] The sulfonated copolyimide was prepared through a high-temperature one-pot polycondensation reaction involving an anhydride and two diamine monomers in a N_2 atmosphere. The polymerization reaction utilized equimolar amounts of two diamines (ODADS and BAPP) and anhydride (NTDA). The sulfonated monomer, ODADS (0.360 g, 1.0 mmol), was dissolved in 3 mL of *m*-cresol with the addition of excess triethylamine (0.24 g, 2.4 mmol) to liberate the amine group and form the zwitterionic form ($NH_4^+SO_3^-$) of ODADS. Following this, other co-monomers, NTDA (0.536 g, 2.0 mmol) and BAPP (0.410 g, 1.0 mmol), and the catalysts, benzoic acid (0.34 g, 2.8 mmol) and isoquinoline (0.33 mL, 2.8 mmol), were added to the reaction mixture with the extra addition of 5 mL of *m*-cresol. After incorporating all the monomers and catalysts, the mixture was stirred at room temperature for 30 minutes and then at 80 °C for 4 h. The formation of polyimide from polyamic acid at this step was achieved by further heating at 180 °C for 20 h. The resulting brown viscous solution was diluted with *m*-cresol at 100 °C and quenched in acetone. The fibrous precipitate was washed several times with acetone and then dried at 80 °C under vacuum for 8 h. The yield of the obtained sulfonated polyimide is 92%. Scheme S1 illustrates the preparation of sulfonated polyimide *via* the chemical imidization of NTDA/ODADS/BAPP.

2.3 Synthesis of HPW@MIL-100(Fe) metal organic framework

Initially, 1.89 g (7.0 mmol) of ferric chloride hexahydrate and 1.36 g (6.4 mmol) of benzene-1,3,5-tricarboxylic acid were dissolved individually in 50 mL of deionized water. The resultant

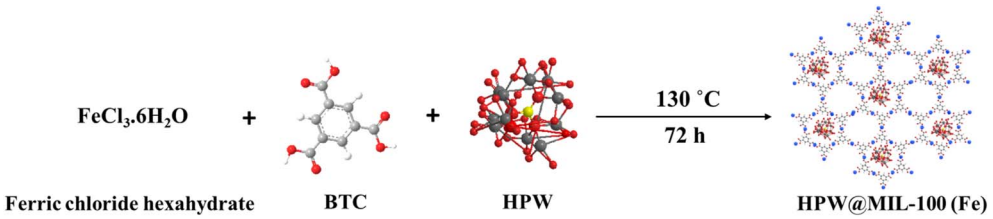

Fig. 1 Schematic of the preparation of HPW@MIL-100(Fe).

solutions were combined by stirring to obtain a clear mixture. An amount of 4.97 g (1.7 mmol) of phosphotungstic acid was added to the homogeneous solution and transferred to a Teflon-lined stainless-steel reactor. The reactor was heated to 130 °C for 72 h. The resultant orange precipitate was washed several times with DI water and ethanol *via* centrifugation and dried under vacuum at 60 °C for 12 h.[26] Fig. 1 displays a pictorial representation of the preparation of HPW@MIL-100(Fe).

2.4 Preparation of sPI and sPI/HPW@MIL-100(Fe) composite membrane

The sPI/HPW@MIL-100(Fe) composite was prepared using the solution casting method. Typically, the Et_3N form of the polymer was dissolved in DMSO (2 wt%), followed by the addition of different loadings (2, 4, 6, and 8 wt%) of HPW@MOF. The mixture was stirred for about 24 h, sonicated, and then cast at 80 °C for a day. The dried membranes were soaked in methanol for 24 h to remove the excess solvent. The membranes underwent acid treatment by immersing in 1.0 M HCl for a full day, followed by thorough washing with deionized (DI) water and drying under vacuum at 150 °C for 20 h. The membrane thickness was found to be between 30 and 50 μm.

2.5 Characterization techniques

2.5.1 Structural analysis. PANalytical (The Netherlands) X-ray diffractometer using Cu Kα radiation in the range of 5–80° 2θ values was employed to obtain the X-ray diffraction pattern of MOF@HPW and composites. Functional groups of the filler and composite were obtained using a Fourier transform infrared (FTIR) spectrometer (Shimadzu IRtracer 100) in the range of 4000–450 cm^{-1}. The ULVAC PHI Versa Probe III (Physical Electronics, USA), which has an Al Kα radiation source, was used to conduct XPS analysis of the high weight percent loaded composite.

2.5.2 Thermal, sorption and mechanical stability analysis. The Netzsch STA 2500 Regulus Thermo Gravimetric Analyzer (TGA) was operated at a heating rate of 10 °C min^{-1} from 30 °C to 800 °C under N_2 atmosphere for thermal stability analysis. The mechanical stability of the composite was tested using a Grayhill (USA) (model ASTM D638) universal testing machine. The N_2 gas adsorption–desorption analysis of the HPW@MIL-100(Fe) was measured using a Quantachrome Novae 2200 instrument. Prior to measurement, the sample was outgassed at 150 °C under vacuum for 12 h and subsequently for 12 h at room temperature.

2.5.3 Morphological and wetting studies. The morphology of HPW@MIL-100(Fe) was analyzed using a JEOL Plus (Japan) high-resolution transmission electron microscope (TEM). The distribution of filler on the polymer surface and the elemental composition of HPW@MIL-100(Fe) were examined using a Thermo Scientific Apreo S (USA) scanning electron microscope (SEM) with energy dispersive X-ray (EDX) mapping. Park Systems Corporation's XE7 Atomic Force Microscope (AFM), in contact mode, was used for the morphological analysis of membranes. The hydrophilic nature of the composite was measured using a Kyowa Interfaces Services contact angle instrument (model: DMS4D7).

2.5.4 Physicochemical studies. The membrane's water uptake and swelling ratio percentages can be determined by eqn (1) and (2), respectively. The water uptake and swelling ratios were analyzed by soaking the membrane in deionized water for 24 h. The weight and thickness of the membrane before soaking were measured and labelled as W_{dry} and T_{dry}, respectively. After the designated time, the membranes were drained and wiped with tissue paper to remove excess water, and W_{wet} and T_{wet} were measured immediately afterwards, where W_{wet} and T_{wet} denote the weight and thickness of the membrane after soaking, respectively, as follows:

$$\text{water uptake}(\%) = \frac{W_{wet} - W_{dry}}{W_{dry}} \times 100, \quad (1)$$

$$\text{swelling ratio}(\%) = \frac{T_{wet} - T_{dry}}{T_{dry}} \times 100. \quad (2)$$

The ion exchange capacity (IEC) was determined by classic acid–base titration between NaCl and NaOH with a phenolphthalein indicator. Eqn (3) was used to calculate the IEC of the membrane samples as follows:

$$\text{IEC(meq per g)} = \frac{V_{NaOH} \times N_{NaOH}}{\text{weight of the polymer}}, \quad (3)$$

where V_{NaOH} is the volume of consumed NaOH and N_{NaOH} is the normality of NaOH used.

The theoretical IEC was calculated using eqn (4) as follows:

$$\text{Ion exchange capacity(meq per g)} = \frac{\text{No. of sulfonic acid groups}(n) \times 1000}{\text{Molecular weight of the repeating unit (Mw)}}. \quad (4)$$

The hydration number defines the ionic interaction between the sulfonic acid group and the water molecules. Eqn (5) was used to calculate the hydration number as follows:

$$\text{Hydration number}(\lambda) = \frac{10}{\text{IEC}} \times \frac{\text{water uptake value}}{18.01}. \quad (5)$$

The oxidative stability of the membrane is assessed by soaking it in a 2 ppm $FeSO_4$ solution containing 3% H_2O_2 (Fenton's reagent). Oxidative stability was calculated using eqn (6) as follows:

$$\text{Oxidative stability}(\%) = \frac{W_a}{W_b} \times 100, \quad (6)$$

where W_b and W_a are the weights of the membrane before and after soaking in Fenton's reagent, respectively.

2.5.5 Electrochemical measurement. The membranes were hydrated with 100% RH for few hours before measurement. The proton conductivity of the membrane was determined using a Zahner impedance analyser at various temperatures, with an AC amplitude of 20 mV and a frequency range of 1–100 kHz. The hydrated membranes were sandwiched between two probe cells placed in the temperature controller. The resistance value of the membrane was determined, and the proton conductivity was calculated using eqn (7) as follows:

$$\sigma(\text{S cm}^{-1}) = \frac{L}{RA}, \quad (7)$$

where L, R and A denote the thickness, resistance and area of the membrane, respectively.

The activation energy (E_a) of the electrolyte membranes was calculated using the linear form of the Arrhenius equation, as follows:

$$\ln(\sigma) = \ln(\sigma_0) - \frac{E_a}{R}\left(\frac{1}{T}\right), \quad (8)$$

where R and T represent the gas constant and temperature, respectively.

2.5.6 Membrane electrode assembly (MEA) fabrication and single-cell testing. The MEA single cell performance was examined at 60 °C and 100% RH using a K-PAS fuel cell station. The catalyst ink was prepared by mixing the powder catalyst (Pt/C, 40 wt%) with a 5% Nafion solution as a binder in a DI water and isopropyl alcohol medium using the ultrasonication method. The catalyst loading was adjusted to 0.6 and 0.8 mg cm^{-2}, and the fuel gas flow rates of H_2 and O_2 were 30 mL min^{-1} and 40 mL min^{-1}, respectively, at the anode and cathode. The 4 wt% sPI/HPW@MIL-100(Fe) MEA with a 9 cm^2 active area was fabricated by applying the hot press method under conditions of 130 °C and 40 bar pressure for 3 min.

3. Results and discussion

3.1 Spectral analysis

The FT-IR spectra of HPW@MIL-100(Fe), sPI, and composites are displayed in Fig. 2. As depicted in Fig. 2(a), for HPW@MIL-100(Fe), the peaks at 1376 cm^{-1} and 1698 cm^{-1} correspond to the stretching vibrations of C–O and C=O bonds of Fe-MOF, respectively.[28] The aromatic C=C bond accounts for the characteristic absorption peaks at 1443 cm^{-1} and 1620 cm^{-1}.[29] The peaks at 809 cm^{-1}, 880 cm^{-1}, 969 cm^{-1}, and 1060 cm^{-1} correspond to the asymmetric stretching vibrations of P–O, W=O, W–O_b–W, and W–O_c–W from phosphotungstic acid, respectively.[30] These vibrations shifted slightly from the vibrational spectrum of bare phosphotungstic acid, confirming its interaction with the organic framework,[31] as shown in Fig. S1. In sPI, sulfonation is confirmed by the S=O stretching peak at 1014 cm^{-1} and a pronounced –OH broad peak around 3500 cm^{-1}. A sharp peak appeared at 1336 cm^{-1}, confirming the C–N stretching. The symmetric and asymmetric stretching vibrations of the C=O group correspond to the peaks noticed at 1659 cm^{-1} and 1711 cm^{-1}, respectively.[32]

As illustrated in Fig. 2(b), the prominent peaks observed around 1336 cm^{-1} and 1659 cm^{-1} are attributed to C–N and C=O stretching vibrations, respectively, in all the composites. This validates that the backbone structure of sPI was not affected by incorporating a filler into the matrices. In addition, the band at 880 cm^{-1} corresponds to the W=O of HPW, which is prominent in all the composites. Additional common peaks of the polymer were also observed, confirming the successful incorporation of the HPW@MIL-100(Fe) into the matrix.

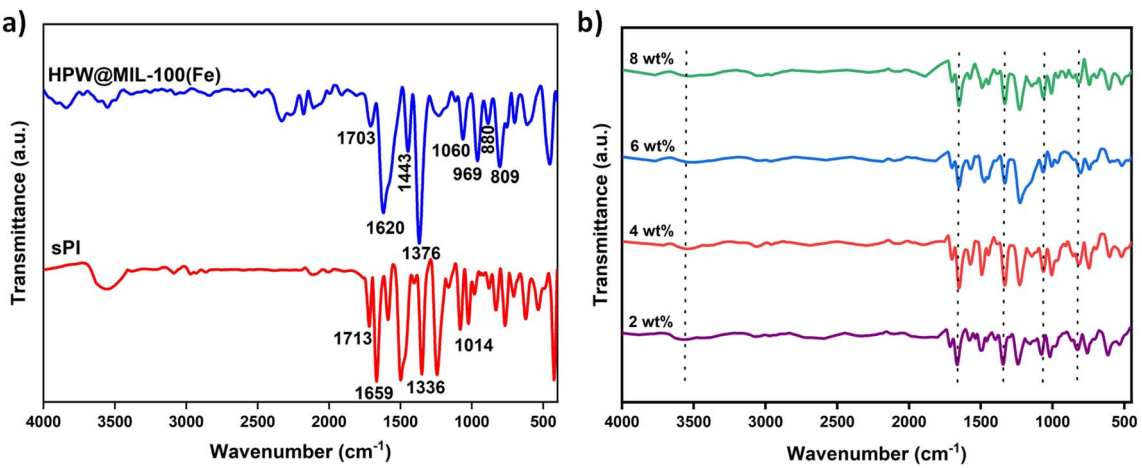

Fig. 2 FT-IR spectra of (a) sPI and HPW@MIL-100(Fe) and (b) sPI/HPW@MIL-100(Fe) (2–8 wt%) composites.

The XRD diffraction pattern of sPI and HPW@MIL-100(Fe) reveals their amorphous and crystalline nature, as shown in Fig. 3(a). The sulfonic acid group grafted onto the side chain of the polymer is responsible for the broader diffraction peak in the vicinity of 20°, indicating amorphous behavior.[33] The broad peak between 5.0° and 8.0° results from the interaction between phosphotungstic acid and MIL-100(Fe). After the addition of HPW onto the MIL-100(Fe) matrix, the electron density of the porous MOF was increased, and the crystal structure of the MOF was not disturbed, which was confirmed by the sharp peaks observed in the diffraction pattern of HPW@MIL-100(Fe).[29,34] The XRD pattern of the composite membranes is displayed in Fig. 3(b). The amorphous nature of the polymer is disturbed by the addition of MOF into the system. The composites seemed to exhibit a semicrystalline behavior. The peak around 10° is preserved in the composite, indicating that the ionic interactions between the polymer and HPW@MOF did not alter the nature of the filler. The characteristic peaks at 21.5°, 33.6°, and 37.1° are attributed to the crystal structure of the MOF preserved in the composite film. Furthermore, a progressive enhancement in peak intensity with increasing additive percentage suggests that the additive is well dispersed and incorporated within the polymer matrix, as confirmed by the XRD results.

The valence state spin–orbit splits for the elements in the sPI/HPW@MIL-100(Fe) composite at 8 wt% were analyzed using XPS. The survey spectra shown in Fig. 4(a) confirmed the presence of elements, such as C, N, O, S, W, and Fe, in the membrane. The C 1 s spectra (Fig. 4(b)) recorded between 280 and 290 eV exhibit three deconvoluted signals at 288.3, 285.8, and 284.9 eV, which correspond to the C–N, C═O, and C═C bonds of the polymer, respectively.[35,36] The sulfonation (C–SO_3H) is confirmed by the S 2p peaks (Fig. 4(c)) deconvoluted at 167.7 eV and 168.9 eV.[37] The N 1s spectrum (Fig. 4(d)) shows a deconvoluted peak at a binding energy of 400.3 eV, which is attributed to the C–N state.[38] The O 1s spectrum displayed in Fig. S2 can be divided into three distinct peaks with binding energies of 531.6, 532.7, and 533.3 eV, indicating the presence of C–O, S–O, and C═O bonds, respectively.[39] The W 4f XPS spectrum (Fig. 4(e)) presents two intense peaks at $4f_{5/2}$ and $4f_{7/2}$, with binding energy peaks centered at 35.7 eV and 37.7 eV, respectively.[40] The deconvoluted peak of W 4f shifts to a lower binding energy than that of WO_3 due to the electron transfer between the tungsten and iron metal ions of the HPW and MOF, respectively.[41] The Fe 2p spectrum exhibits two distinct peaks at 711.3 and 724.6 eV, accompanied by satellite peaks corresponding to the Fe $2p_{3/2}$ and Fe $2p_{1/2}$ binding energy levels, respectively, which are attributed to the Fe^{3+} state.[42] The XPS analysis results are comparable and consistent with the FT-IR spectra.

3.2 Morphological analysis

The structural morphology of the synthesized HPW@MIL-100(Fe), sPI and composite membranes was investigated, and the images are shown in Fig. 5. The structure of the prepared HPW@MOF, as displayed in Fig. 5(a) and (b), showed octahedral geometry with the distribution of phosphotungstic acid groups on the matrices. The obtained morphology agrees with previous studies.[26] The average particle size of the filler is found to be 75 nm. The EDX spectrum depicted in Fig. S3 shows elements such as C, O, P, Fe, and W, which confirms the successful incorporation of the HPW into the MIL-100(Fe)

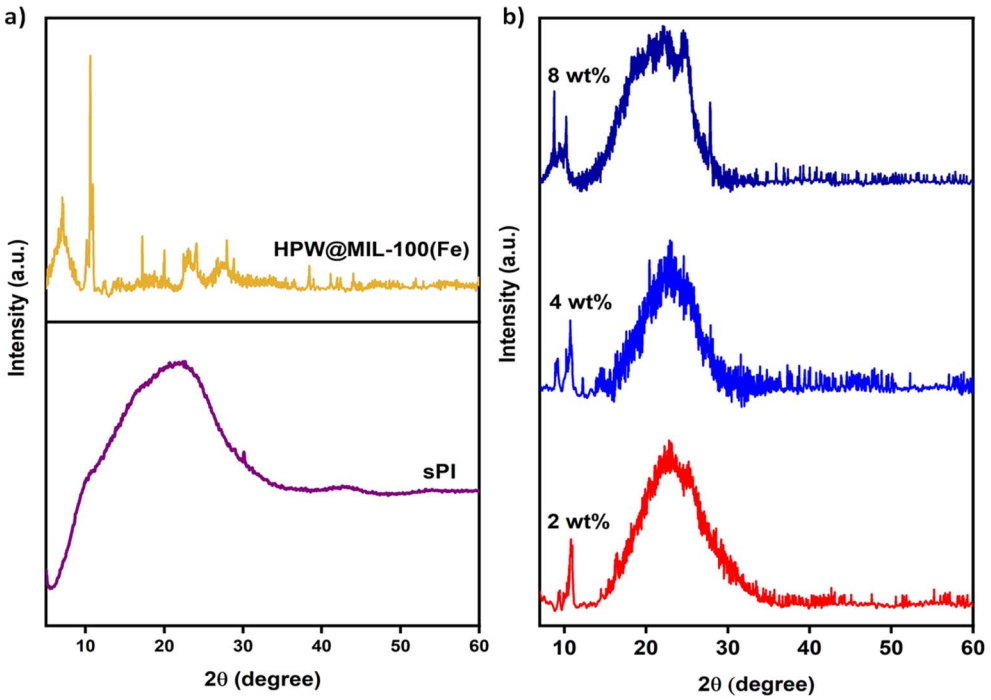

Fig. 3 XRD patterns of (a) sPI and HPW@MIL-100(Fe) and (b) sPI/HPW@MIL-100(Fe) (2, 4, and 8 wt%) composites.

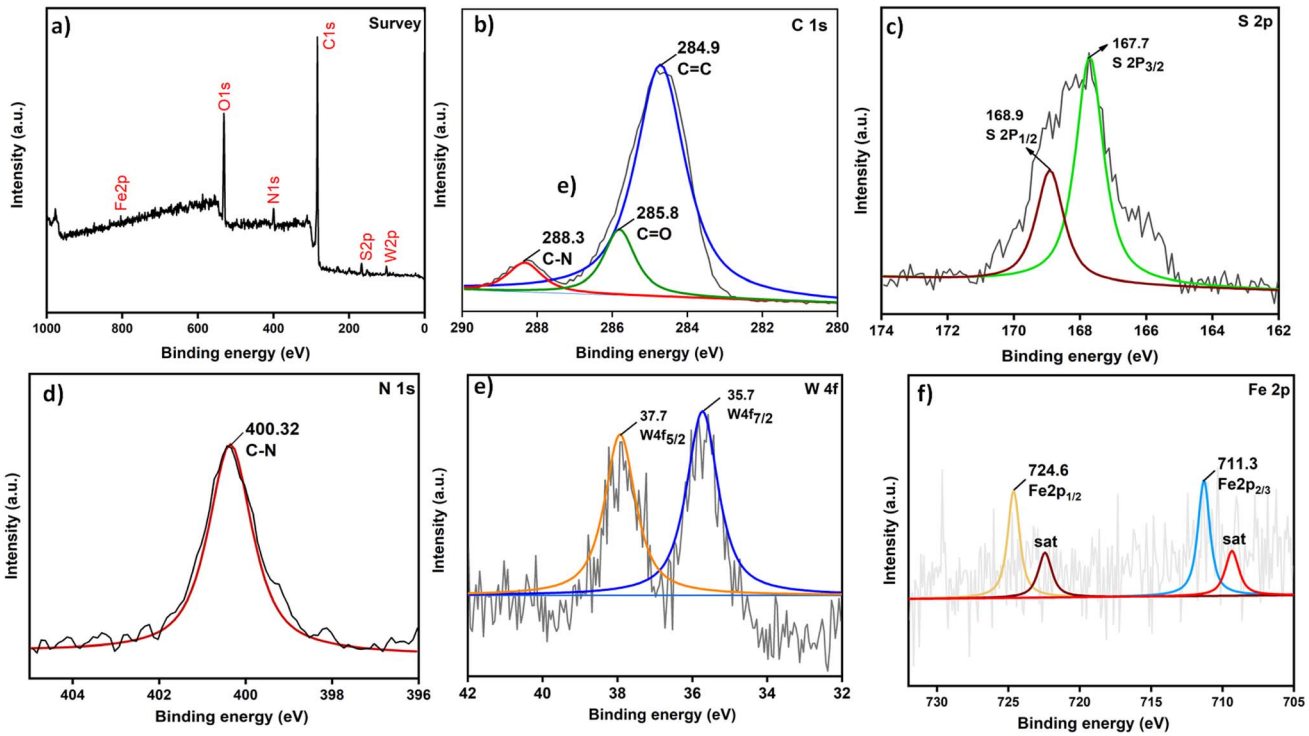

Fig. 4 XPS spectra of (a) survey (b) C 1s (c) S 2p (d) N 1s (e) W 4f and (f) Fe 2p in sPI/HPW@MIL-100(Fe) (8 wt%) composite membrane.

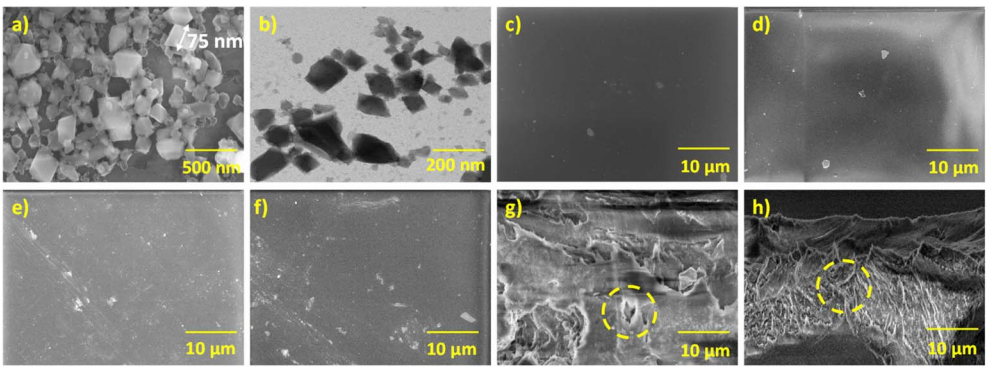

Fig. 5 (a and b) SEM and TEM images of HPW@MIL-100(Fe). (c–f) Surface SEM images of sPI and sPI/HPW@MIL-100(Fe) at 2, 4 and 8 wt% loading. (g and h) Cross-section SEM images of sPI/HPW@MIL-100(Fe) at 4 and 8 wt% loading.

cavities. In addition to EDX confirmation, elemental mapping in SEM analysis displayed in Fig. S4 supports the presence of these elements in HPW@MIL-100(Fe).

The pristine sPI exhibited a smooth surface, as shown in Fig. 5(c). With an increase in the filler concentration, the smoothness of the surface is altered with an increase in roughness. The sPI/HPW@MIL-100(Fe) composites with 2 wt%, 4 wt% and 8 wt% loading show regular distribution of HPW@MIL-100(Fe) onto the polymer matrix displayed in Fig. 5(d–f). It is observed that the uniformity of the membrane is not affected after the HPW@MIL-100(Fe) loading onto the bare sPI matrix. The cross-section images for the composites are displayed in Fig. 5(g and h). In a 4 wt% membrane matrix, the porous nature of the material is apparent, which is ascribed to filler loading that increases the material's perviousness and helps in proton conduction. With the increase in the HPW@MIL-100(Fe) concentration, the agglomeration of the particles, which block the porous strands of the membrane, was observed to retard the performance of the composite. The cross-section SEM images at higher magnification are displayed in Fig. S5.

The topographical environment of the composites was studied using AFM, as shown in Fig. S6. Contact mode 3D images clearly show the distribution of the HPW@MOF on the polymer matrix. The AFM height images of the sPI/HPW@MIL-100(Fe) composite membranes show light and dark phase separation. The carbon backbone of the polymer structure is responsible for the light areas, and the dark areas are attributable to the moieties of the polymer ($-SO_3H$) and filler in micrographic images.[43,44] The 4 wt% sPI/MIL-100(Fe) composite

shows a well-dispersed and even loading of the filler in the polymer matrix. In the 8 wt% loaded membrane (Fig. S6(c) and (f)), large clusters were observed, which is due to the aggregation of the moieties that retard the performance of the composite.

3.3 Chemical stability and sorption analysis

The chemical stability of the NTDA/ODADS/BAPP polymer was assessed by immersing it in 12 M HCl, 3 M NaOH, and MeOH for 7 days. As displayed in Fig. S7 and S8, all the membranes immersed in their respective media show no changes in physical appearance. After this period, the membrane soaked in acid and base media exhibits high structural integrity without compromising the mechanical properties. This is not the case for the membrane soaked in MeOH, which cracked after treatment. The FT-IR analysis displayed in Fig. S9 shows that the important functional group bonds, like S=O (1014 cm^{-1}), C–N (1336 cm^{-1}), and C=O (1659, 1711 cm^{-1}) bonds, were not disturbed, no bond shift was observed, and the polymer's structure was preserved. Though the membrane soaked in methanol broke after treatment, the major groups were not disturbed, and solubility was not observed in any medium. This reflects a positive response to the stability of the polymer. The porous nature of the prepared HPW@MIL-100(Fe) was measured by N_2 sorption analysis. Fig. S10 displays the adsorption–desorption isotherms; both MIL-100(Fe) and HPW@MIL-100(Fe) show mesoporous behaviour of exhibiting a type 4 isotherm. The Brunauer–Emmett–Teller (BET) surface area of the prepared HPW@MIL-100(Fe) is 63.52 $m^2\ g^{-1}$, which is lower than that of MIL-100(Fe) (414.90 $m^2\ g^{-1}$). This reduction demonstrates the successful incorporation of HPW into the frameworks of MIL-100(Fe).

3.4 Physicochemical studies

The membrane's ion exchange capacity, along with changes in weight and thickness when exposed to an aqueous medium, was measured, as shown in Table 1. The composite's water uptake capacity and swelling ratio depend on the hygroscopic behavior of the sulfonic acid moieties of the pristine polymer. Both WU and SR show a similar increasing trend with an increase in filler concentration. This is evident for two reasons: (i) the presence of hydrophilic functional groups, –COOH, –OH, and $–SO_3H$, in both the pristine and filler matrices, and (ii) the porous nature of the MIL-100(Fe), which increases the water absorption capacity of the hybrid membranes.[45–47] The combined effect of both factors results in water uptake values ranging from 11.48% to 14.47% at 30 °C and from 16.43% to 21.86% at 60 °C, which is higher than that of the pristine sPI. The obtained water uptake values fell within a range that did not deteriorate the mechanical properties and dimensional stability of the matrix membranes.

The movement and penetration of the solvent molecules are the major reasons for the swelling behaviour of the polymeric membrane. Compared to the pristine sPI, the composite membrane exhibits a lower swelling ratio, which can be attributed to (i) electrostatic interactions between the polymer and the filler matrix and (ii) the rigid structure of the MOF that restricts the segmental motion of the water molecules.[48,49] The swelling ratio increases with an increase in temperature, and a maximum swelling of 23.33% at 60 °C is observed for 2 wt% loaded sPI. Overall, the relatively low swelling behaviour of these composite membranes suggests their suitability as proton exchange membranes for fuel cell applications.

The ion exchange capacity of the conductive membrane is directly proportional to the mass fraction of the ionizable sulfonic acid groups within the membranes.[50] The IEC of the pristine sPI is measured to be 1.66 meq per g, which is comparable with the theoretical IEC value. The theoretical IEC value for the prepared sPI polyimide was calculated using eqn (4). For sPI, $n = 2$ and Mw is 1265 g mol^{-1}. Substituting the values in eqn (4), the obtained theoretical IEC is 1.59 meq per g. As the concentration of the HPW@MIL-100(Fe) filler within the polymer matrix increases, the IEC of the membrane increases. This enhancement is attributed to the carboxyl and hydroxyl groups found in the filler, which increase the number of exchangeable groups in the hybrid membranes. Moreover, the super acidity of phosphotungstic acid adds extra H^+, further elevating the IEC.[51,52] The IEC increases up to 4 wt% and then declines, likely due to the aggregation of the filler in the polymer matrix, which obstructs the functional groups from engaging in exchange during titration. The hydration number (λ) for sPI and composite membranes was calculated from the measured IEC and water uptake values. For a pristine membrane, the λ value is 3.43, while the sPI/HPW@MIL-100(Fe) membrane (2–8 wt%) has a λ value ranging from 3.76 to 4.18. It is noteworthy that all the physicochemical properties show the same trend for all the composites.

Table 1 Physicochemical characterization of the sPI and sPI/HPW@MIL-100(Fe) composites

	Water uptake (%)		Swelling ratio (%)		IEC (meq per g)	Hydration number
Membrane code	30 °C	60 °C	30 °C	60 °C	30 °C	30 °C
sPI	10.26	14.45	12.90	21.42	1.66	3.43
sPI/HPW@MIL-100(Fe) (2 wt%)	12.83	17.28	14.77	23.33	1.73	4.11
sPI/HPW@MIL-100(Fe) (4 wt%)	14.47	21.86	13.09	20.18	1.92	4.18
sPI/HPW@MIL-100(Fe) (6 wt%)	13.23	19.07	11.76	16.04	1.88	3.90
sPI/HPW@MIL-100(Fe) (8 wt%)	11.48	16.43	10.20	12.81	1.70	3.76

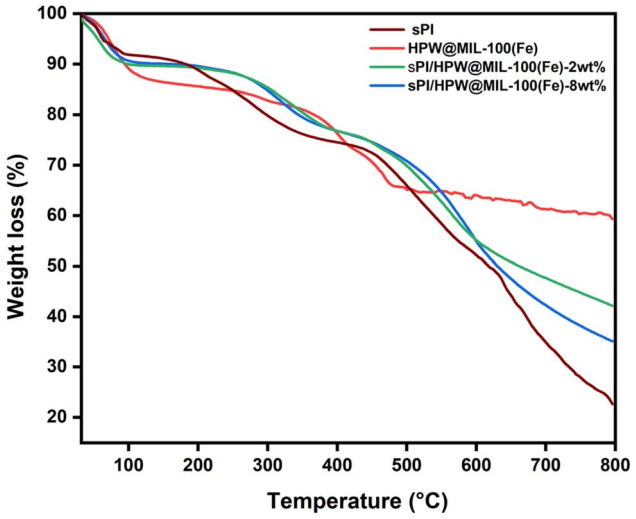

Fig. 6 Thermal stability curves of the sPI, HPW@MIL-100(Fe) and sPI/HPW@MIL-100(Fe) composites.

3.5 Thermal and oxidative stability

The TGA thermograms for pristine sPI, HPW@MIL-100(Fe) and composite membranes are displayed in Fig. 6. In pristine sPI, the initial 10% weight loss is observed due to the moisture content in the polymer. The second weight loss results from the degradation of the hydrophilic sulfonic acid segment. Finally, the deterioration of the aromatic backbone is noted above 450 °C, with nearly 80% of the polymer degrading around 800 °C. The sPI matrix shows high thermal stability, and this degradation pattern is comparable to the other reported NTDA-ODADS-based polyimides.[53] The filler HPW@MIL-100(Fe) exhibits a three-step degradation process; the first weight loss, occurring around 100 °C, is attributed to the loss of water molecules. The second weight loss stems from the coordinated water molecules bound to the metal atoms. The third step of degradation is due to framework implosion and the breakdown of the ligand moiety.[26]

In the composite membrane, the weight loss observed above 100 °C, following the evaporation of water molecules, results from the degradation of the functional moieties of both the polymer and filler. The thermal stability displayed above 200 °C for the composites is higher than that of the pristine sPI, which is attributed to electrostatic interactions between the MOF and polymer. Above 600 °C, the sPI loaded with 8 wt% HPW@MIL100(Fe) shows a comparatively higher percentage weight loss than the 2 wt% loaded sPI due to the effect of filler agglomeration in the polymer matrices.[54,55]

The peroxide radical attack on the composite membrane was evaluated by immersing the sPI/HPW@MIL-100(Fe) composite membranes in Fenton's reagent at 80 °C (Fig. S11). The immersion period was one hour, and the difference in membrane weight was assessed to calculate oxidative stability. The results indicate a decrease in the weight loss percentage as the HPW@MIL-100(Fe) loading increases. This is attributed to the protection of the sulfonic acid group of the polymer ($-SO_3H$) from the $^{\bullet}OH$ and $^{\bullet}OOH$ radicals by the ionic groups of the HPW@MIL-100(Fe). The shelter effect arises from the formation of hydrogen bonds between the filler and the polymer.[56] A greater shielding effect was observed in the 4 wt% loaded composites, which show an oxidative stability (OS) of 88.13%, surpassing that of the 2 wt% loading. However, beyond this increase in weight loading percentage, a deviated proclivity is observed due to aggregation. These results indicate that these composites possess sufficient oxidative stability and are suitable for PEMFC applications.

3.6 Mechanical stability and contact angle measurements

The prepared composite membranes were subjected to measurements of tensile strength and contact angle, and the results are displayed in Fig. S11 and 7, respectively. The electrostatic interactions between the polymer and filler and hydrophilic functional groups in the composites were the key driving forces for these measurements. With an increase in the filler concentration, the tensile strength value increases, and the composite membranes show values in the range of 12.63–23.55 MPa. The highest value was shown by the 4 wt% loaded composite, which is about twice that of the pristine material, and the highly loaded composite exhibits a lower tensile strength value. The increased strength value of the hires is due

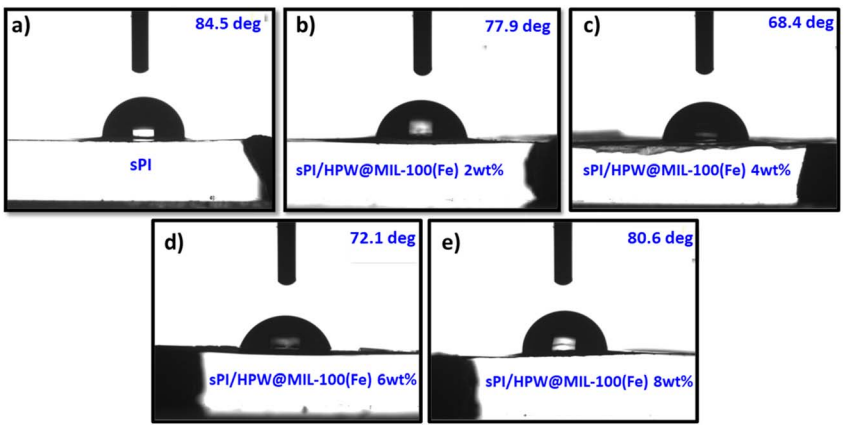

Fig. 7 Hydrophilic behavior of the (a) sPI and (b–e) sPI/HPW@MIL-100(Fe) (2–8 wt%) composites.

to factors such as electrostatic ionic interactions between the –SO_3H groups of the polymer and the –OH groups of the filler.[57] The tensile strength value decreases after 4 wt% extra addition, and this is due to the aggregation of the filler on the polymer matrices, which retards the flexibility and increases the brittleness of the composite.[58]

The presence of hydrophilic moieties in the composites can significantly influence the proton conduction behaviour of the composites. The contact angle of the membranes was measured to quantify hydrophilic behaviour. The pristine membrane was found to have a contact angle of 84.5 deg., as shown in Fig. 7(a). With an increase in HPW@MIL-100(Fe) concentration, the contact angle decreased, indicating increased hydrophilicity.[59] This trend was observed for only the 2 wt% and 4 wt% loadings displayed in Fig. 7(b and c). Beyond this, at 6 wt% and 8 wt% loadings, the contact angle increased again, as shown in Fig. 7(d and e), due to agglomeration. This effect increases surface roughness and area, decreases wettability, and reduces the water-holding capacity in the composites, which is reflected as an increased contact angle measurement.

3.7 Electrochemical studies

The proton conductivity of pristine sPI and sPI/HPW@MIL-100(Fe) composite membranes with 2–8 wt% loading was measured at various temperatures (30 °C–80 °C), as displayed in Fig. 8. The proton conductivity of the pristine membrane is measured to be 0.023 S cm^{-1} at 30 °C, and this value tends to increase with the loading of HPW-encapsulated MOF. The sPI membrane loaded with 4 wt% HPW@MOF shows the maximum proton conductivity of 0.046 S cm^{-1} under the same conditions. This increase is attributed to the following reasons: (i) the porous nature of the MIL-100(Fe) increases the number of proton conductive sites; (ii) the high-density phosphate groups in phosphotungstic acid possess good conductive properties and interact with water molecules, aiding proton transport; and (iii) in addition to phosphate groups, hydroxyl groups in the super acid further enhance proton conduction channels by forming dense hydrogen bonding networks on the MIL-100(Fe) channels.[60–62] However, with a further increase in loading percentage, the value begins to decrease due to the aggregation of the filler within the polymer matrix.

The positive effect of temperature on the pristine sPI and composite membranes was studied, and the trend was the same as that observed at RT. The proton conductivity of these membranes shows doubled time-enhanced activity with an increase in temperature. This is because of an increase in the mobility of the conduction species with increased heating.[63] At 80 °C, a 4 wt% loaded sPI membrane produced the highest proton conductivity of 0.085 S cm^{-1}, while pristine sPI showed a conductivity of 0.048 S cm^{-1}. Despite aggregation, the composite membranes loaded with 6 wt% and 8 wt% showed higher proton conductivity than that of the pristine.

The temperature-dependent conductivity of the membranes follows the Arrhenius equation. The activation energy values are shown in Fig. 8(b). The E_a values for the composites are lower than those of the pristine matrix. The sPI and hybrid membranes exhibit E_a values ranging from 11.36 to 14.99 kJ mol^{-1}. These values indicate that both the Grotthuss and vehicular mechanisms facilitate the conduction of protons. The vehicular mechanism is enhanced by the conduction of protons through water molecules. Using this mechanism, the proton transported as the Grotthuss mechanism is driven by the sulfonic acid moieties and functional groups of the filler. The water molecules absorbed by the polymer matrix lay the foundation for the hydrogen bond network in the MIL-100(Fe) MOF, which facilitates proton hopping. In addition, the dense hydrogen networks formed between the phosphate and sulfonate groups further decrease the activation energy for proton conduction, thereby increasing the conductivity.[64,65] The conduction mechanism in sPI/HPW@MIL-100(Fe) composites is displayed in Fig. 9.

3.8 Fuel cell performance

The sPI pristine matrix loaded with 4 wt% of HPW@MIL-100(Fe) demonstrated a proton conductivity of 0.085 S cm^{-1} at 80 °C, which is higher than that of the other composites

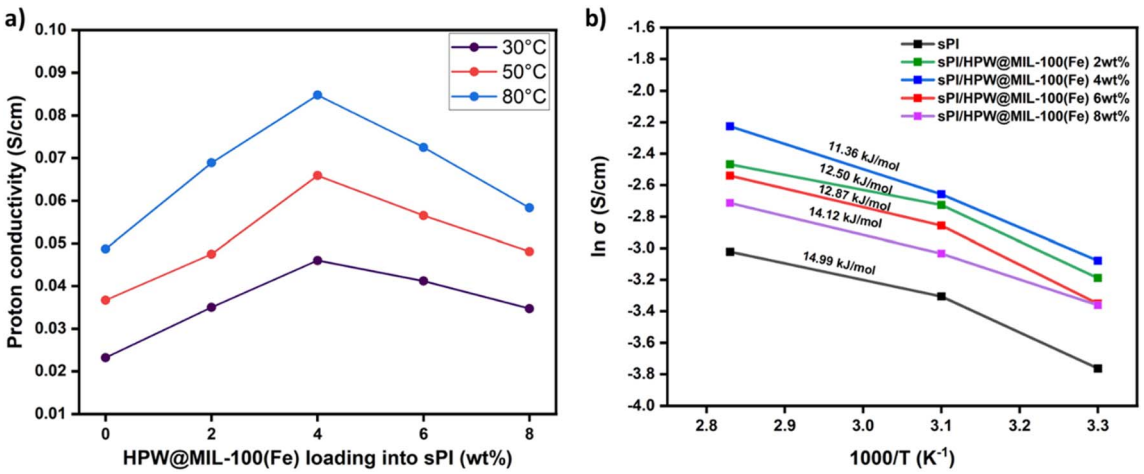

Fig. 8 (a) Proton conductivity and (b) Arrhenius plots of the sPI and sPI/HPW@MIL-100(Fe) composites at various temperatures.

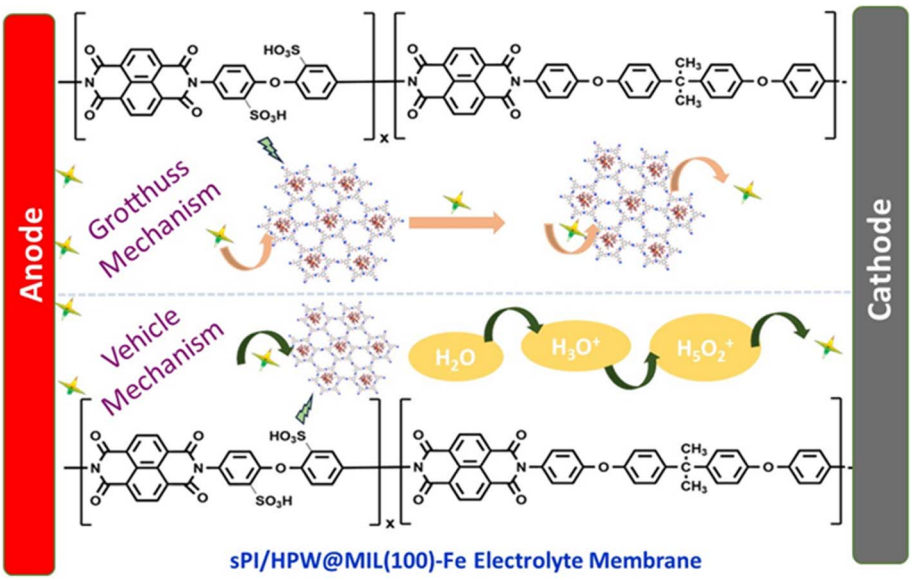

Fig. 9 Mechanism of proton transport in the sPI/HPW@MIL-100(Fe) composites.

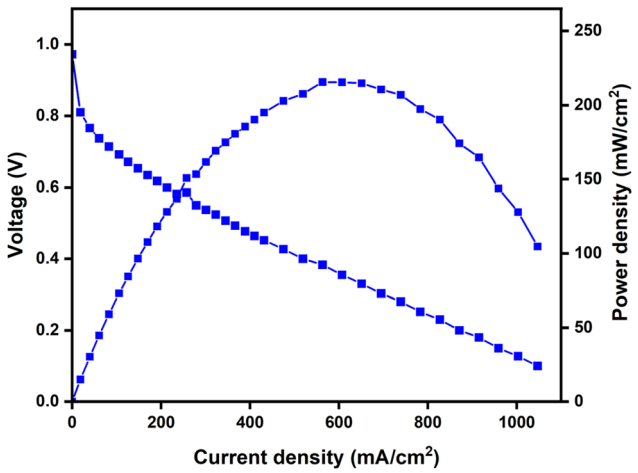

Fig. 10 Fuel cell performance of the sPI/HPW@MIL-100(Fe) (4 wt%) composite membrane.

subjected to single-cell performance applications. As the temperature increased, the peak power density also increased. The fuel cell performance at the optimal condition of 60 °C is shown in Fig. 10. The bare sPI exhibited a maximum power density of 63 mW cm^{-2},[14] while sPI/HPW@MIL-100(Fe) (4 wt%) membrane achieved a maximum power density of 216 mW cm^{-2} with an open circuit voltage (OCV) of 0.972 V. This enhanced performance was attributed to synergistic Grotthuss and vehicular mechanisms. From this result, it can be concluded that sPI/HPW@MIL-100(Fe) with 4 wt% loading exhibits better performance than the sPI membrane. The significant improvement indicates that the HPW@MOF-loaded sPI is a suitable candidate for PEMFC applications.

4. Conclusion

In summary, we report for the first time the incorporation of phosphotungstic acid immobilized on an iron framework into a sulfonated polyimide matrix. The composite membranes were produced using the solution casting technique. The sPI/HPW@MIL-100(Fe) composites exhibited enhanced physicochemical and electrochemical properties compared to the pristine membrane. All notable properties improved with an increase in the addition of MOF, but this trend continued only up to 4 wt% loading. Beyond this concentration, a decline in water uptake, IEC, and conductivity is likely due to the filler aggregation phenomenon. At 80 °C, the sPI/HPW@MIL-100(Fe) composite with 4 wt% loading achieved a maximum proton conductivity of 0.085 S cm^{-1}, which is nearly twice that of the pristine matrix (0.048 S cm^{-1} under the same conditions). The synergistic effects of the porous nature of the MOF, the ionic functionalities in HPW, and the hydrophilic groups of the polymer contribute to this enhancement. Furthermore, fabricated sPI/HPW@MIL-100(Fe) MEA with 4 wt% loading delivered a peak power density of 216 mW cm^{-2} at 60 °C under 100% relative humidity. These findings highlight that immobilized heteropolyacids loaded onto sulfonated polyimide can lead to significant advancements in PEMFC applications.

Author contributions

Ragasudha Sudhakaran: conceptualization, data curation, writing – original draft, methodology, and investigation. Preethi Dayalan: conceptualization, methodology, and investigation. Paradesi Deivanayagam: conceptualization, resources, supervision, and writing – review and editing.

Conflicts of interest

The authors declare that there are no known competing financial interests.

Data availability

The data supporting this study will be made available upon request to the corresponding author.

Supplementary information (SI): chemical imidization of the NTDA/ODADS/BAPP-based sulfonated polyimide, FT-IR spectra of HPW and HPW@MIL-100(Fe), XPS spectra of O 1s, EDX spectrum of HPW@MIL-100(Fe), elemental mapping of HPW@MIL-100(Fe), Cross-section SEM images under higher magnification, AFM images of sPI/ HPW@MIL-100(Fe) with 2, 4, and 8 wt% loading, Digital images of the sPI membrane soaked in 12 M HCl, 3 M NaOH, and MeOH at varied periods of 24 h, 72 h, 96 h, 144 h and 168 h, Physical stability of the membrane, FT-IR spectra of the membranes after chemical treatment, N_2 adsorption–desorption isotherms of MIL-100(Fe) and HPW@MIL-100(Fe), oxidative stability of the composites and mechanical stability of the sPI/HPW@MIL-100(Fe) composites. See DOI: https://doi.org/10.1039/d6ra01800a.

Acknowledgements

One of the authors (RS) acknowledges the University Grants Commission, the Government of India (UGC-SJSGC), for the funding to carry out this research work (UGCES-22-OB-TAM-F-SJSGC-7008). All authors sincerely thank the SRM Central Instrumentation Facility (SCIF), the Nanotechnology Research Centre (NRC) and the Department of Chemistry, SRMIST, Kattankulathur, Tamil Nadu, India, for providing the instrumentation facilities to characterize the membranes.

References

1 K. Qiao, H. Liu, K. Ren, P. Sun, L. Yang, S. Wang and D. Cao, *Sustain. Energy Fuels*, 2023, **7**, 1829–1838, DOI: 10.1039/D2SE01675C.
2 P. Kulasekaran, B. M. Mahimai and P. Deivanayagam, *RSC Adv.*, 2020, **10**(44), 26521–26527, DOI: 10.1039/D0RA04360E.
3 S. J. Jang, Y. K. Jung, J. H. Lee, S. H. Lee, T. H. Shin and Y. W. Lee, *RSC Adv.*, 2026, **16**(12), 10925–10934, DOI: 10.1039/d5ra08718j.
4 M. Kesava and K. Dinakaran, *Int. J. Hydrogen Energy*, 2021, 1121–1132, DOI: 10.1016/j.ijhydene.2020.09.117.
5 N. A. H. Rosli, K. S. Loh, W. Y. Wong, R. M. Yunus, T. K. Lee, A. Ahmad and S. T. Chong, *Int. J. Mol. Sci.*, 2020, **21**, 632, DOI: 10.3390/ijms21020632.
6 M. S. Mohy Eldin, A. E. Hashem, T. M. Tamer, A. M. Omer, M. E. Yossuf and M. M. Sabet, *Int. J. Electrochem. Sci.*, 2017, **12**, 3840–3858, DOI: 10.20964/2017.05.45.
7 M. Kamal, J. Jaafar, A. A. Khan, Z. Khan, A. F. Ismail, M. H. D. Othman, M. A. Rahman, F. Aziz and G. U. Rehman, *Energy Fuels*, 2024, **38**, 12337–12386, DOI: 10.1021/acs.energyfuels.4c00462.
8 K. Hooshyari, M. B. Karimi, H. Su, S. Rahmani and H. R. Rajabi, *Int. J. Energy Res.*, 2022, **46**, 9178–9193, DOI: 10.1002/er.7794.
9 Z. Wang, J. Zhang, S. Lu, Y. Xiang, Z. Shao and S. P. Jiang, *Adv. Sustain. Syst.*, 2023, **7**, 2200432, DOI: 10.1002/adsu.202200432.
10 E. Kowsari, A. Zare and V. Ansari, *Int. J. Hydrogen Energy*, 2015, **40**, 13964–13978, DOI: 10.1016/j.ijhydene.2015.08.064.
11 K. Wei, F. Zhai, X. Lu, L. Zhuang and S. Zhao, *Ind. Eng. Chem. Res.*, 2025, **64**, 6519–6529, DOI: 10.1021/acs.iecr.4c04746.
12 B. K. Chen, T. Y. Wu, C. W. Kuo, Y. C. Peng, I. C. Shih, L. Hao and I. W. Sun, *Int. J. Hydrogen Energy*, 2013, **38**, 11321–11330.
13 P. Sarkar, A. K. Mohanty, P. Bandyopadhyay, S. Chattopadhyay and S. Banerjee, *RSC Adv.*, 2014, **4**, 11848–11858, DOI: 10.1039/c3ra46528d.
14 R. Sudhakaran, S. Moorthy and P. Deivanayagam, *Energy Fuels*, 2025, **39**, 15474–15488, DOI: 10.1021/acs.energyfuels.5c01755.
15 X. Guo, F. Zhai, J. Fang, M. F. Laguna, M. Lopez-Gonzalez and E. Riande, *J. Phys. Chem. B*, 2007, **111**, 13694–13702, DOI: 10.1021/jp0734631.
16 B. M. Mahimai, P. Kulasekaran, G. Sivasubramanian and P. Deivanayagam, *Polym. Plast. Tech. Mat.*, 2020, **59**, 1791–1800, DOI: 10.1080/25740881.2020.1765385.
17 W. Nimir, A. Al-Othman, M. Tawalbeh, A. A. Makky, A. Ali, H. Karimi-Maleh and C. Karaman, *Int. J. Hydrogen Energy*, 2023, **48**, 6638–6656, DOI: 10.1016/j.ijhydene.2021.11.174.
18 M. T. Musa, N. Shaari and S. K. Kamarudin, *Int. J. Energy Research*, 2021, **45**, 1309–1346, DOI: 10.1002/er.5874.
19 B. M. Mahimai, G. Sivasubramanian, S. Moorthy and P. Deivanayagam, *Ind. Eng. Chem. Res.*, 2022, **61**, 8081–8090, DOI: 10.1021/acs.iecr.2c01209.
20 S. Moorthy, R. Sudhakaran, A. Mahalingam, H. Pushparaj and P. Deivanayagam, *Ind. Eng. Chem. Res.*, 2024, **63**, 17567–17576, DOI: 10.1021/acs.iecr.4c02057.
21 M. Kourasi, R. G. A. Wills, A. A. Shah and F. C. Walsh, *Electrochim. Acta*, 2014, **127**, 454–466, DOI: 10.1016/j.electacta.2014.02.006.
22 N. Esmaeili, E. M. A. Gray and C. J. Webb, *Chem. Phys. Chem.*, 2019, **20**, 2016–2053, DOI: 10.1002/cphc.201900191.
23 M. Zeng, W. Liu, H. Guo, T. Li, Q. Li, C. Zhao and H. Li, *ACS Appl. Energy Mater.*, 2022, **5**, 9058–9069, DOI: 10.1021/acsaem.2c01503.
24 S. Zaidi, S. Mikhailenko, G. Robertson and S. Kaliaguine, *J. Memb. Sci.*, 2000, **178**, 17–34, DOI: 10.1016/S0376-7388(00)00345-8.
25 P. Molla-Abbasi, K. Janghorban and M. S. Asgari, *Iranian Polym. J.*, 2018, **27**, 77–86, DOI: 10.1007/s13726-017-0587-0.
26 R. Canioni, C. Roch-Marchal, F. Sécheresse, P. Horcajada, C. Serre, M. Hardi-Dan, G. Férey, J. M. Grenèche, F. Lefebvre, J. S. Chang, Y. K. Hwang, O. Lebedev, S. Turner and G. Van Tendeloo, *J. Mater. Chem.*, 2011, **21**, 1226–1233, DOI: 10.1039/c0jm02381g.
27 Z. Zhang, J. Ren, J. Xu, L. Meng, P. Zhao and Z. Wang, *Int. J. Hydrogen Energy*, 2020, **45**, 27527–27538, DOI: 10.1016/j.ijhydene.2020.07.027.

28 M. Chen, J. Yan, Y. Tan, Y. Li, Z. Wu, L. Pan and Y. Liu, *Ind. Eng. Chem. Res.*, 2015, **54**, 11804–11813, DOI: 10.1021/acs.iecr.5b02746.
29 F. Zhang, Y. Jin, J. Shi, Y. Zhong, W. Zhu and M. S. El-Shall, *Chem. Eng. J.*, 2015, **269**, 236–244, DOI: 10.1016/j.cej.2015.01.099.
30 D. Jin, Z. Hou, Y. Luo and X. Zheng, *J. Mol. Catal. A Chem.*, 2006, **244**, 233–238, DOI: 10.1016/j.molcata.2005.08.037.
31 A. E. R. S. Khder, H. M. A. Hassan and M. S. El-Shall, *Appl. Catal. A Gen.*, 2014, **487**, 110–118, DOI: 10.1016/j.apcata.2014.09.018.
32 T. Ryu, S. C. Sutradhar, F. Ahmed, K. Choi, H. Yang, S. Yoon and S. Lee, *J. Ind. Eng. Chem.*, 2017, **47**, 99–104, DOI: 10.1016/j.jiec.2017.01.013.
33 J. B. A. J. H. Therese, R. Gayathri, K. Selvakumar, M. R. Prabhu and P. Sivakumar, *Mater. Res. Express*, 2019, **6**, 11, DOI: 10.1088/2053-1591/ab4a3b.
34 Z. Zhang, J. Ren, J. Xu, L. Meng, P. Zhao, H. Wang and Z. Wang, *J. Memb. Sci.*, 2021, **622**, 119304, DOI: 10.1016/j.memsci.2021.119304.
35 F. Ekiz, F. Ouzkaya, M. Akin, S. Timur, C. Tanyeli and L. Toppare, *J. Mater. Chem.*, 2011, **21**, 12337–12343, DOI: 10.1039/c1jm12048d.
36 S. Theerthagiri, I. B. Rachman, M. S. Islam, J. Y. Park and S. J. Song, *ACS Appl. Polym. Mater.*, 2025, 3954–3967, DOI: 10.1021/acsapm.5c00196.
37 S. Moorthy and P. Deivanayagam, *ACS Appl. Mater. Interfaces*, 2024, **16**, 14712–14721, DOI: 10.1021/acsami.3c17299.
38 H. Ji, H. Ju, R. Lan, P. Wu, J. Sun, Y. Chao, S. Xun, W. Zhu and H. Li, *RSC Adv.*, 2017, **7**, 54266–54276, DOI: 10.1039/c7ra10697a.
39 Z. Guo, J. Chen, J. J. Byun, R. Cai, M. Perez-Page, M. Sahoo, Z. Ji, S. J. Haigh and S. M. Holmes, *J. Energ. Chem.*, 2021, **61**, 323–334, DOI: 10.1016/j.jechem.2021.04.061.
40 M. Mazur, D. Wojcieszak, A. Wiatrowski, D. Kaczmarek, A. Lubańska, J. Domaradzki, P. Mazur and M. Kalisz, *Appl. Surf. Sci.*, 2021, **543**, 151151, DOI: 10.1016/j.apsusc.2021.151151.
41 P. Chatterjee, D. Piecha, S. Kotarba, K. Syrek, M. Pisarek and G. D. Sulka, *ACS Appl. Mater. Interfaces*, 2025, 30284–30296, DOI: 10.1021/acsami.5c03437.
42 Y. Wang, W. Guo, X. Li and N. Y. Kang, *RSC Adv.*, 2018, **8**, 36477–36483, DOI: 10.1039/C8RA07007E.
43 G. Wang, S. Yang, N. Y. Kang, B. Hua, M. Lu, H. Wei and Y. M. Lee, *Macromolecules*, 2023, **56**, 5546–5556, DOI: 10.1021/acs.macromol.3c00301.
44 B. Xue, Z. Zheng, H. Qian, Z. Wang and J. Yan, *Macromolecules*, 2024, **57**, 3376–3386, DOI: 10.1021/acs.macromol.4c00117.
45 A. Msahel, F. Galiano, M. Pilloni, F. Russo, A. Hafiane, R. Castro-Muñoz, V. B. Kumar, A. Gedanken, G. Ennas, Z. Porat, A. Scano, S. B. Hamouda and A. Figoli, *Membranes*, 2021, **11**, 1–18, DOI: 10.3390/membranes11010065.
46 J. Canivet, A. Fateeva, Y. Guo, B. Coasne and D. Farrusseng, *Chem. Soc. Rev.*, 2014, **43**, 5594–5617, DOI: 10.1039/c4cs00078a.
47 Y. Fang, Z. Yang, H. Li and X. Liu, *Environ. Sci. Pollut. Res.*, 2020, **27**, 4703–4724, DOI: 10.1007/s11356-019-07318-w.
48 M. H. Eikerling and P. Berg, *Soft Matter*, 2011, **7**, 5976–5990, DOI: 10.1039/c1sm05273j.
49 K. D. Kreuer, *J. Memb. Sci.*, 2001, **185**, 29–39, DOI: 10.1016/S0376-7388(00)00632-3.
50 D. Paradesi, D. Samanta, A. B. Mandal and S. N. Jaisankar, *RSC Adv.*, 2014, **4**(50), 26193–26200, DOI: 10.1039/C4RA00904E.
51 Y. Li, H. Wang, Q. Wu, X. Xu, S. Lu and Y. Xiang, *Electrochim. Acta*, 2017, **224**, 369–377, DOI: 10.1016/j.electacta.2016.12.077.
52 H. Wu, X. Wu, Q. Wu and W. Yan, *Compos. Sci. Technol.*, 2018, **161**, 1–6, DOI: 10.1016/j.compscitech.2018.04.018.
53 B. R. Einsla, Y. T. Hong, Y. S. Kim, F. Wang, N. Gunduz and J. E. Mcgrath, *J. Polym. Sci. Pol. Chem.*, 2004, **42**, 862–874, DOI: 10.1002/pola.11026.
54 V. J. Pastore, T. R. Cook and J. Rzayev, *Chem. Mater.*, 2018, **30**, 8639–8649, DOI: 10.1021/acs.chemmater.8b03881.
55 E. George, J. Joy, H. Vahabi, S. C. George and S. Anas, *Nano-Struct. Nano-Objects*, 2024, **38**, 101372, DOI: 10.1016/j.nanoso.2024.101372.
56 S. Mukhopadhyay, A. Das, T. Jana and S. K. Das, *ACS Appl. Energy Mater.*, 2020, **3**, 7964–7977, DOI: 10.1021/acsaem.0c01323.
57 X. Guo, Z. Zhang, Z. Liu, H. Huang, C. Zhang and H. Rao, *Nanomaterials*, 2024, **14**, 1217, DOI: 10.3390/nano14141217.
58 Y. H. Shih, G. L. Chen, P. H. Liu, K. W. Tseng, W. Y. Lee, W. C. Chen, L. Wang and C. C. Chueh, *ACS Appl. Electron. Mater.*, 2024, **6**, 1797–1808, DOI: 10.1021/acsaelm.3c01719.
59 E. Ahmed, A. A. Farghali and M. F. Hmamm, *RSC Adv.*, 2025, **15**(36), 29777–29798, DOI: 10.1039/D5RA03667D.
60 L. Xu, J. Xu, M. Liu, H. Han, H. Ni, L. Ma and Z. Wang, *Int. J. Hydrogen Energy*, 2015, **40**, 7182–7191, DOI: 10.1016/j.ijhydene.2015.02.139.
61 R. Vani, S. Ramaprabhu and P. Haridoss, *Sustain. Energy Fuels*, 2020, **4**, 1372–1382, DOI: 10.1039/C9SE01031A.
62 P. Li, H. Guo, Y. Lv, L. Zhang, P. Sun and Z. Li, *ACS Appl. Energy Mater.*, 2022, **5**, 4956–4969, DOI: 10.1021/acsaem.2c00333.
63 J. Jiang, X. Zhu, H. Qian, J. Xu, Z. Yue, Z. Zou and H. Yang, *Sustain. Energy Fuels*, 2019, **3**, 2426–2434, DOI: 10.1039/C9SE00318E.
64 H. Wu, X. Shen, Y. Cao, Z. Li and Z. Jiang, *J. Memb. Sci.*, 2014, 74–84, DOI: 10.1016/j.memsci.2013.09.058.
65 M. Yamada and I. Honma, *J. Phys. Chem. B*, 2006, **110**, 20486–20490, DOI: 10.1021/jp063488k.